



Enabling the activation of lattice oxygen and high distribution of Co^{3+} on LaCoO_3 surface through fluorine incorporation to promote toluene combustion

Bing Li^a, Hao Xiong^a, Weili Dai^{a,*}, Zhilong Huang^a, Xiaolian Zhong^a, Jie Zhang^a, Lei Zhou^a, Keshi Wu^{b,c,**}, Jianping Zou^a, Xubiao Luo^{a,d}

^a Key Laboratory of Jiangxi Province for Persistent Pollutants Control and Resources Recycle, Nanchang Hangkong University, Nanchang, Jiangxi 330063, China

^b All-China Environment Federation, China

^c School of Environmental and Chemical Engineering, Shanghai University, Shanghai 200444, China

^d School of Life Science, Jinggangshan University, Ji'an 343009, China

ARTICLE INFO

Keywords:

Perovskite oxide
F incorporation
Lattice oxygen activation
Abundant Co^{3+}
Toluene adsorption

ABSTRACT

Limited by the sluggish oxygen mobility, perovskite catalysts are still unsatisfactory in real application. Herein, an effective strategy concerning the activation of surface lattice oxygen in LaCoO_3 via fluorine incorporation was proposed to improve its toluene oxidation performance. The constructed LCO-2 F reveals more outstanding catalytic activity than that of bare LCO, and excellent long-term run along with water-resistance. Concretely, the F incorporation results in the reduced electronic density around surface lattice oxygen together with the weakened Co–O bond strength, and thus the enhanced surface lattice oxygen activity. Moreover, the F incorporation promotes the exposure of more electron-deficient Co^{3+} species accompanying with abundant surface lattice oxygen as well, which contribute to the adsorption and activation of toluene. In situ DRIFTS results indicate that LCO-2 F also possesses superior O_2 replenishing capacity for fast degradation regarding the tough intermediate species of benzoate, and thus speeding the catalytic cycle.

1. Introduction

Volatile organic compounds (VOCs), as a type of prevailing pollutant, have brought about extensive concern due to their intrinsic toxicity and deuterogenic contaminants, such as photochemical smog, tropospheric ozone as well as fine particulate matter (PM_{2.5}), which severely endanger the ecological environment and human body [1–3]. Therefore, more stringent emission standards are being implemented worldwide. Eco-friendly and efficient means for VOCs abatement is imperative. Among diverse methods, catalytic oxidation draws more attention as a result of its advantages of energy conservation, high-efficiency and no secondary contamination [4]. Apparently, catalyst plays a vital role to eliminate VOCs upon catalytic oxidation. Given that the noble metal catalysts are featured by the scarcity and ease of inactivation at high temperatures, perovskite oxides with the general formula ABO_3 have been considered as potential alternatives for catalytic removal of VOCs, primarily due to their low cost, good thermal

stability as well as tunable activity for catalytic oxidation [5]. Generally, catalytic oxidation of VOCs over a perovskite oxide obeys the Mars-van Krevelen (MvK) mechanism, where the surface lattice oxygen plays a vital role in deep oxidation of VOCs [6,7]. However, perovskite oxides are always fabricated at high temperatures, which lead to an inferiorly intrinsic activity characterized by sluggish lattice oxygen mobility. Accordingly, exploring a straightforward and efficient strategy to activate the lattice oxygen of perovskite oxide is crucial for improving its catalytic oxidation performance towards VOCs.

Fortunately, perovskite oxides possess greatly structural flexibility for regulating the lattice oxygen activity [8]. In virtue of this merit, numerous strategies by constructing the structural defects as partially substitution of the A or the B cation with other cations [9–13] and modulation of non-stoichiometric composition with A cation defects [14–16] have been adopted to indirectly facilitate the lattice oxygen mobility of perovskite oxides. However, the forthright scheme for the lattice oxygen activation is that decrease the charge density of lattice

* Corresponding author.

** Corresponding author at: All-China Environment Federation, China.

E-mail addresses: wldai81@126.com (W. Dai), wks@vocs-china.com (K. Wu).

<https://doi.org/10.1016/j.apcatb.2024.123828>

Received 9 November 2023; Received in revised form 18 January 2024; Accepted 6 February 2024

Available online 8 February 2024

0926-3373/© 2024 Elsevier B.V. All rights reserved.

oxygen to form the electron-deficient oxygen species, namely electrophilic oxygen O^{2-x} , which is more favor to accelerate the oxidation of VOCs molecules [17,18]. Nevertheless, at present, more strategies to directly activate the lattice oxygen upon the reduction of charge density are that create the heterogeneous interface between two metal oxides. For instance, Wang et al. [18] reconstructed the $La_{0.3}Sr_{0.7}CoO_3$ by ethylene glycol dissolution to generate the $Co_3O_4/La_{0.3}Sr_{0.7}CoO_3$ interface, which triggers the transfer of electrons in lattice oxygen of $La_{0.3}Sr_{0.7}CoO_3$ into Co_3O_4 , resulting in more formation of active lattice oxygen. Hence, broadening the methodology for activating the lattice oxygen in perovskite oxide by lowering its charge density is of great theoretical and practical importance. It was documented that fluorine with the high electronegativity can affect the electronic properties of catalysts [19,20]. Therefore, incorporation fluorine ions into the perovskite oxide lattice may hold promise to lower the charge density of lattice oxygen and thus generate more active lattice oxygen, ascribed to the strong electrophilic ability of fluorine. Whereas, such work has yet been reported in the aspect of VOCs oxidation.

Herein, the fluorine incorporated $LaCoO_3$ catalysts were constructed by hydrothermal method combining with thermal calcination, and applied for the catalytic combustion of toluene. The fluorine ions were doped into $LaCoO_3$ lattice to substitute the oxygen ions. The results of experimental characterization and theoretical calculation presented that the surface lattice oxygen in fluorine substituted $LaCoO_3$ catalysts was successfully activated, attributing to the reduced electronic density around lattice oxygen and weakened Co–O bond strength. Moreover, highly distributive surface Co^{3+} species were unexpectedly generated that promoted the adsorption and activation of toluene molecules. Consequently, the $LaCoO_3$ catalyst with a proper fluorine substitution revealed the elevated catalytic activity and satisfactory stability with long-term run as well considerable resistance against 10 vol% H_2O .

2. Experimental

2.1. Preparation of catalysts

All analytical grade reagents were used without further purification. For preparation of pristine $LaCoO_3$, 5 mmol of $La(NO_3)_3 \cdot 6 H_2O$ (Adamas) and 5 mmol of $Co(NO_3)_2 \cdot 6 H_2O$ (Adamas-beta) were dissolved in 20 mL of deionized water with magnetic stirring to form a homogeneous solution, and followed by addition of ethylenediamine tetracetic acid (EDTA) (20 mmol, Adamas) and citric acid (20 mmol, Adamas) under a unremitting stirring for 6 h. After that, the dispersion liquid (solution A) was transferred to a 100 mL of Teflon-lined autoclave and maintained at 160 °C for 10 h. The resultant suspension was dried at 80 °C overnight and subsequently calcined at 900 °C for 2 h with a heating rate of 2 °C·min⁻¹ in the muffle furnace to get the final $LaCoO_3$ that abbreviated to LCO. For the fabrication of F substituted $LaCoO_3$, the identical process was adopted except addition of NH_4F (Adamas) with diverse amount of 1.5 mmol, 2 mmol and 2.5 mmol into the solution A, respectively. The obtained catalysts were labelled as LCO-xF, where x refers to the dosage of NH_4F in the synthesis process.

2.2. Characterization of catalysts

The characterization including the X-ray diffraction, Raman spectroscopy, Fourier transform infrared spectroscopy, transmission electron microscopy, high-resolution transmission electron microscopy, X-ray photoelectron spectroscopy, electron paramagnetic resonance, H_2 temperature programmed reduction (H_2 -TPR) and O_2 temperature programmed desorption (O_2 -TPD), toluene-TPD, contact angle measurement as well as in situ diffuse reflectance infrared Fourier transform spectroscopy were performed. The details of various characterization were revealed in the [Supplementary Information](#).

2.3. Evaluation of catalytic performance

The catalytic performance of the as-synthesized LCO catalysts for the complete toluene oxidation were performed in a fixed-bed quartz microreactor with inner diameter of 6 mm. A catalyst of 100 mg (40–60 mesh) was used for each test. Typically, a feed gas containing 1000 ppm of toluene was generated through a bubbler equipped with liquid toluene in a thermostatic bath with the air as balance gas, and the total gas flow rate was 100 mL/min. The concentration of toluene and CO_2 was detected by a gas chromatograph (GC-7920) equipped with two flame ionization detectors, respectively. To estimate the influence of water vapor on the catalytic activity, 10 vol% of H_2O was injected to the feed gas by a pump during the process of stability test. The calculations in terms of the toluene conversion, CO_2 yield, activation energy, along with reaction rate were presented in the [Supplementary Information](#).

2.4. DFT calculations

The density functional theory (DFT) calculations were carried out using Vienna Ab initio Simulation Package (VASP) with the functional of Perdew-Burke-Ernzerhof (PBE) of generalized gradient approximation (GGA) to represent the electron exchange-correlation. Setting 400 eV cut-off energy for the plane-wave. The convergence criterion for the electronic relaxation and ionic optimizations was set to 10^{-4} eV and 0.02 eV Å⁻¹, respectively. The k-points meshing for Brillouin zone was set as $7 \times 7 \times 3$ for bulk $LaCoO_3$ and $3 \times 3 \times 1$ for the slab. The calculation details were presented in the [Supplementary Information](#).

3. Results and discussion

3.1. Structural and morphological characterization

The crystal structure of $LaCoO_3$ and F substituted $LaCoO_3$ catalysts was examined by the X-ray diffraction (XRD) technique. As presented in [Fig. 1a](#), the main peaks of all as-synthesized catalysts are indexed to the pure $LaCoO_3$ crystalline phases (PDF#48–0123) [21]. No fluorine-containing species can be detected. More importantly, the (012) diffraction peaks in the patterns of F substituted $LaCoO_3$ present obvious right-shifting, suggesting that F is doped into the $LaCoO_3$ lattice and partially replaces the lattice O^{2-} because of the smaller ionic radius of F^- (1.33 Å) than that of O^{2-} (1.40 Å) [22], thus resulting in the shrinkage of crystal lattice with a reduction in the crystal grain sizes ([Table S1](#)). However, more incorporation of F into the LCO lattice (LCO-2.5 F) results in a slight left-shifting in the case of the (012) diffraction peak. This may be due to that the superfluous fluorine are positioned on the interstitial lattice of LCO that accordingly causes a marginal expansion of the LCO-2.5 F lattice and the diffraction peak shifts towards lower angle relative to LCO-2 F [23]. In addition, the status of F anion in the LCO-2 F catalyst was further clarified by FT-IR analysis ([Fig. S1](#)). The two prominent peaks located at 580 and 667 cm⁻¹ present the Co–O stretching vibration mode in perovskite $LaCoO_3$ [24]. Specially, an exclusive peak at 755 cm⁻¹ is found in LCO-2 F, which ascribes to the stretching of M–F (La–F and Co–F) bond [25], further demonstrating the undoubted substitution of O^{2-} by F^- in $LaCoO_3$ lattice. The Raman spectral profile recorded for $LaCoO_3$ ([Fig. 1b](#)) exhibited three main peaks at around 465, 507, and 672 cm⁻¹, which can be ascribed to the semiconducting state, E_g quadrupole mode of $LaCoO_3$, and Co–O stretching vibration, respectively [26]. It is accepted that the position of Co–O stretching vibration peak is related to the variation in average length of Co–O bond, which may result from the epitaxial strain-induced structure distortion of CoO_6 regular octahedrons [27]. With the fluorine incorporation, the position of Co–O stretching vibration over LCO-2 F catalysts is red-shifted, which indicates an increase in the mean Co–O bond length. The variational Co–O bond strength can be distinctly recognized by the bond force constant (k) calculated by the equation of

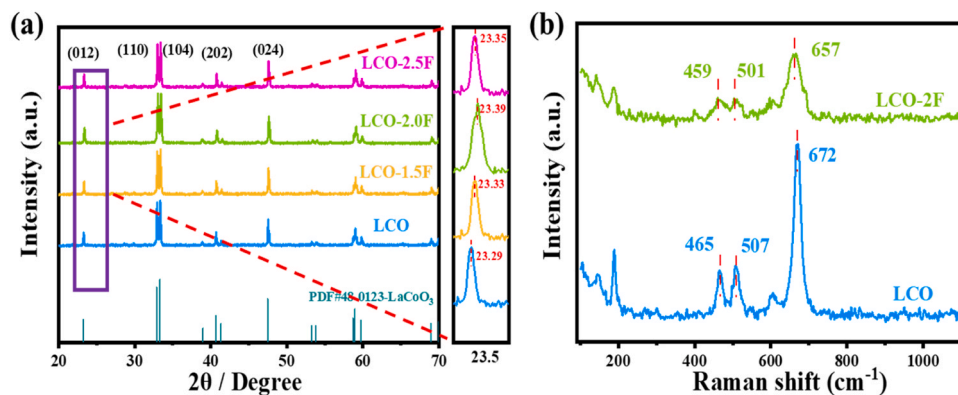


Fig. 1. (a) XRD patterns of all catalysts and (b) Raman spectra of LCO and LCO-2 F.

$\omega = \frac{1}{2\pi c} \sqrt{\frac{k}{\mu}}$, where ω is the Raman shift (cm^{-1}), c is light velocity, and μ is reduced mass of Co and O atom [28]. As depicted in Fig. S2, the k value reduces from 335.0 to 320.2 N/m with the F substitution. The attenuated Co–O bond strength could heighten the migration of the lattice oxygen over LCO-2 F.

Fig. 2 reveals the morphological and crystal lattice difference of LaCoO_3 -based catalysts before and after F incorporation. Both of LCO and LCO-2 F present an irregular accumulation of nanoparticles (Fig. 2a and c), which conforms to the representative morphological feature of La-based perovskite due to the high temperature treatment during preparation process. However, the mean particle size of LCO-2 F is smaller than that of LCO (29.87 nm vs. 42.38 nm, inset of Fig. 2a and c), which is in line with the results of crystal grain sizes. The HRTEM images (Fig. 2b and d) exhibit evident interplanar spacing of approximately 0.38 and 0.28 nm, corresponding to the (012) and (110) faces of the LaCoO_3 crystal phase, respectively [26]. Apparently, the interplanar spacing decreases after F doping, meaning a lattice shrinkage of LCO-2 F arising from the F incorporation. Meanwhile, no impurity related to fluoride can be observed. The EDS elemental mapping images illustrate that O, Co, La, and F are distributed uniformly on the LCO-2 F without the isolated F species. Above results is in well consistent with the XRD result. The N_2 adsorption-desorption isotherms with a type IV isotherm

of the as-resulted catalysts are presented in Fig. S3, suggesting the mesoporous structure [29]. In addition, the specific surface area (SSA) and total pore volume of all catalysts are given in Table S1. The SSA and pore volume of LCO increase following the F incorporation, which would contribute to more active sites exposed on the catalysts surface and thus improve the catalytic activity.

3.2. Surface composition and chemical state

To illustrate the influence of F incorporation on the surface composition and chemical state of LaCoO_3 , XPS experiment was conducted and the results were shown in Fig. 3 and Fig. S4. Compared to pristine LCO, an additional peak at around 684 eV appears in the survey spectra of F substituted LCO that refers to the characteristics of F, which demonstrates the successful introduction of F once more. As exhibited in Fig. 3a, La 3d spectra depicts two major doublets at around 834.2 and 851.5 eV, which can be distributed to the $\text{La } 3d_{5/2}$ and $\text{La } 3d_{3/2}$ orbitals, respectively [30]. The peak position of F substituted LCO visibly shifts to higher binding energy compared to that of pristine LCO, signifying that the electron density around La reduces, which results from the formation of La–F bond and the electron-withdrawing ability of highly electro-negative F. This result is also verified by the FT-IR analysis. The Co 2p spectra, as presented in Fig. 3b, shows a multiple splitting at

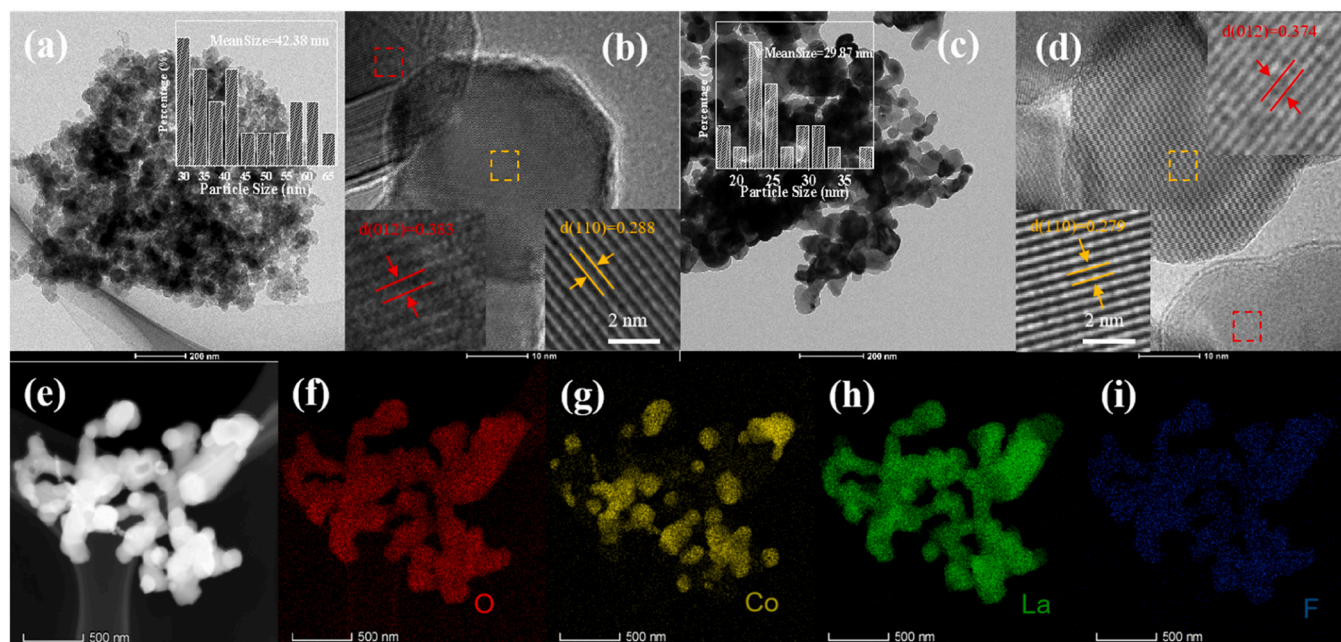


Fig. 2. TEM and HRTEM images of (a–b) LCO and (c–d) LCO-2 F, and (e–i) elemental mapping images of LCO-2 F.

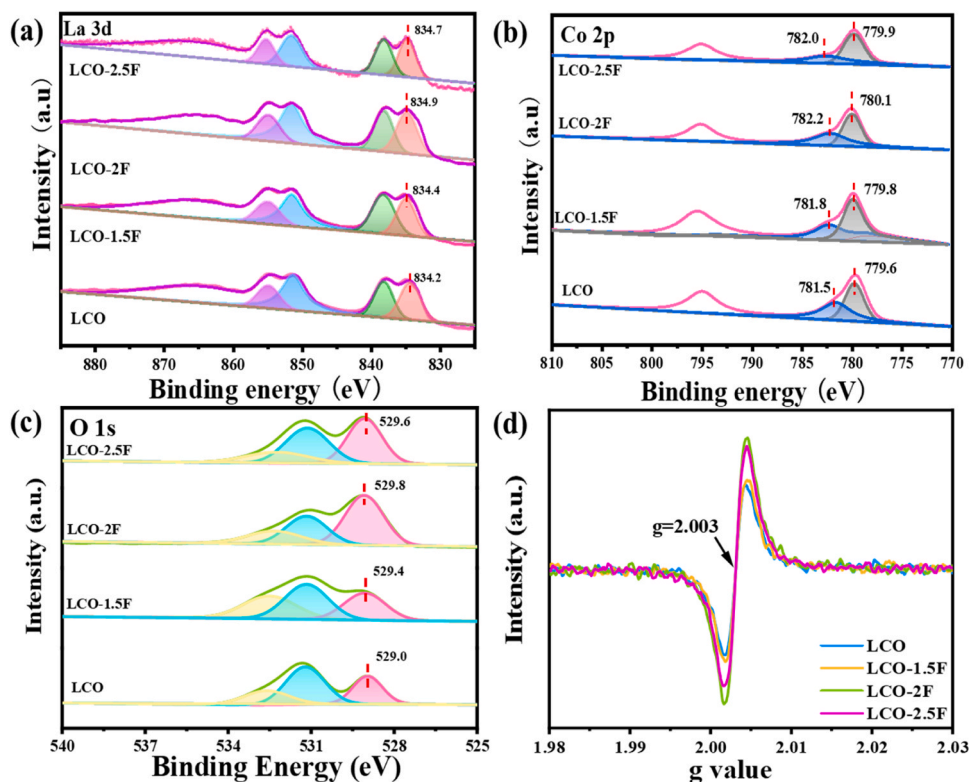


Fig. 3. XPS spectra of (a) La 3d, (b) Co 2p and (c) O 1 s for LCO and LCO-F, (d) EPR spectra for LCO and LCO-F.

approximately 795.0 and 779.6 eV, assigning to Co 2p_{1/2} and Co 2p_{3/2} level, respectively [31]. Besides, the overlapped Co 2p_{3/2} spectra can be fitted into Co³⁺ and Co²⁺ spin doublets, which corresponds to the binding energy of about 779.6 and 781.5 eV, respectively. Parallely, the binding energy of Co 2p also presents a positive shift as the identical reason. Expressly, LCO-2 F exhibits a greater shift, which may be ascribed to the closer bond between Co and F, and thus generating the weaker Co–O bond strength. Meanwhile, the Co³⁺/Co²⁺ ratios were calculated based on the corresponding peak area and summarized in Table S1, which follow the sequence of LCO < LCO-1.5 F < LCO-2.5 F < LCO-2 F, suggesting that F incorporation increases the content of the Co³⁺ species and LCO-2 F distributes more Co³⁺ species on the surface. Since the surface Co³⁺ species act as the active sites during the catalytic oxidation of hydrocarbon, abundant Co³⁺ species can promote the adsorption and activation of hydrocarbon [15,32]. Besides that, the F incorporation also enables the surface reconstruction over LCO with decreased surface La/Co ratio (Table S1). According to the previous literature [33], the greater electronegativity difference between two elements, the stronger bond strength of a polar covalent bond. Consequently, The La–F bond should present a strong binding strength than that of Co–F bond based on the electronegativity of F (3.98), La (1.1) and Co (1.9) [34]. Moreover, more F ions are incorporated into the bulk of LCO (as discussed hereinbelow). Hence, more F ions could more easily combine with La ions rather than Co ions in the bulk of LCO, which leads to more La ions existed in the bulk, and thus decreasing the surface La/Co ratio. This results in more exposure of active Co species and thus enhance the catalytic performance. More importantly, to investigate the electronic structure of surface O_{latt} in F substituted LaCoO₃, the asymmetrical O 1 s spectra can be deconvoluted into three peaks (Fig. 3c). The peaks at approximately 529.0 eV, 531.1 eV and 532.5 eV are ascribed to surface O_{latt}, surface-adsorbed oxygen species (O_{ads}) stemmed from surface oxygen vacancies and the adsorbed OH groups, respectively [35,36]. Notably, the peaks of surface O_{latt} are significantly shifted to higher binding energy after F incorporation, meaning a lower electron density, which helps to improve the activity of surface O_{latt} [18,

37]. Similar phenomenon can also be found in previous report [25]. Generally, the surface O_{latt} species function as the active oxygen species to dominate the catalytic oxidation of VOCs followed the MvK mechanism. Accordingly, the surface O_{latt}/O_{ads} ratios are figured up and presented in Table S1. The O_{latt}/O_{ads} ratios increase with F incorporation and rank in the order of LCO (0.69) < LCO-1.5 F (0.91) < LCO-2.5 F (1.10) < LCO-2 F (1.65), which is in line with the the abundance of surface Co³⁺ species due to the electroneutrality and in contrast with the strength of Co–O bond. Distinctly, LCO-2 F has a more plentiful surface O_{latt}, which will contribute to the improvement of catalytic activity in VOCs combustion. In a word, F incorporation results in more abundance of Co³⁺ species and activated surface O_{latt} in LaCoO₃, which could greatly enhance its catalytic capacity toward VOCs oxidation.

To evaluate the overall oxygen vacancies concentration and furture explain the state of F existed in LaCoO₃ structure, EPR characterization was carried out. As shown in Fig. 3d, as-prepared catalysts present a symmetric EPR signal at around g = 2.003, signifying the existence of oxygen vacancies [38]. The quantity of overall oxygen vacancies first increases with the content of F increase and then decreases. LCO-2 F reveals the largest amount of overall oxygen vacancies. It is documented that if F dopes on the metal oxide surface, there will be more surface oxygen vacancies generated [19]. Nevertheless, LCO-2 F possesses highest oxygen vacancies concentration, but least surface O_{ads} species that directly refer to the surface oxygen vacancies. Accordingly, it is easy to speculate that more bulk oxygen vacancies exist in LCO-2 F resulted from incorporation F into LCO lattice. It was reported that bulk oxygen vacancies could accelerate the transfer of bulk O_{latt} species to surface and thus also favor of VOCs combustion [39].

3.3. Catalytic performance for toluene oxidation

The catalytic performance of LCO and F substituted LCO for the total oxidation of toluene were assessed. The behaviors of toluene conversion as a function of reaction temperature are shown in Fig. 4a. The temperatures regarding 50, 90 and 100% toluene conversion (T₅₀, T₉₀ and

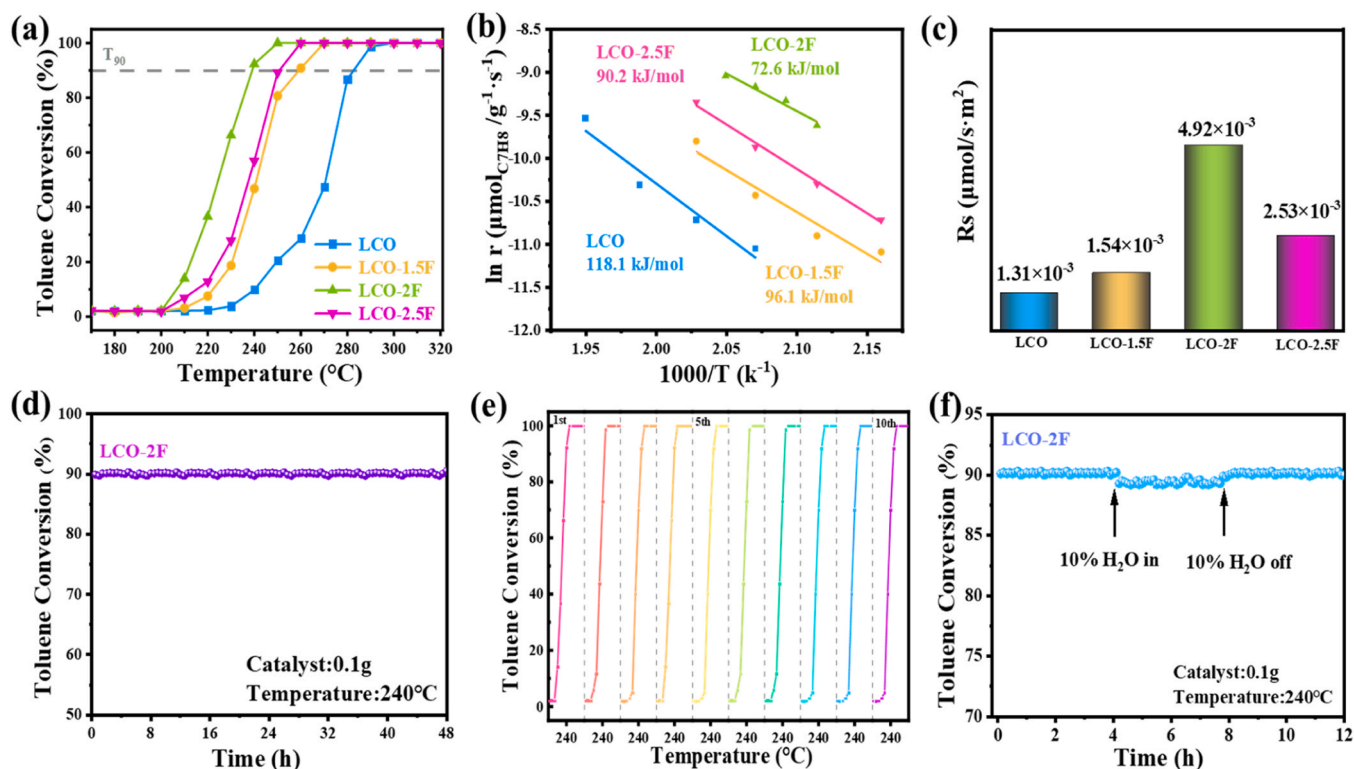


Fig. 4. (a) Catalytic performance of the as-prepared catalysts, (b) Arrhenius plots of the catalysts, (c) Specific reaction rate of catalysts, (d) Catalytic stability for LCO-2 F, (e) Cycle tests for LCO-2 F over 10 cycles, and (f) Water resistance of LCO-2 F.

T_{100}) are summarized in Table 1. Apparently, the toluene conversion monotonously raises with the reaction temperature and a total oxidation of toluene can be readily reached below 250 °C over F substituted LaCoO_3 , while the pristine LaCoO_3 requires nearby 300 °C to achieve the complete toluene conversion. Furthermore, The T_{50} is 271, 239, 226, and 235 °C for LCO, LCO-1.5 F, LCO-2 F, and LCO-2.5 F, respectively, and corresponding T_{90} locates at 283, 251, 238, and 246 °C. Obviously, F incorporation markedly elevates the toluene conversion efficiency and the variation of toluene conversion presents a volcano shape with the additive amount of F. The curves of CO_2 yield are basically coincident with those of toluene conversion (Fig. S5), implying the outstanding mineralization ability for toluene. In this work, LCO-2 F with a right amount of F incorporation exerts the best activity for toluene combustion,

but the excessive F addition could be detrimental to certain extent.

Generally, toluene oxidation under the oxygen-rich atmosphere would obey a first-order kinetic mechanism [40]. The Arrhenius plots of $\ln r$ vs $1000/T$ for the toluene conversion at less than 20% were drawn in Fig. 4b. The E_a values increase following the order of LCO-2 F (72.6 kJ/mol) < LCO-2.5 F (90.2 kJ/mol) < LCO-1.5 F (96.1 kJ/mol) < LCO (118.1 kJ/mol), which are well consistent with their corresponding catalytic activity. LCO-2 F has a much lower E_a value, demonstrating its better catalytic ability for toluene oxidation. To eliminate the influence of SSA on catalytic activity, the specific reaction rate (R_s) of as-fabricated catalysts at 210 °C are calculated and shown in Fig. 4c and

Table 1
Toluene oxidation activity, specific reaction rate (R_s), apparent activation energies (E_a) of the Catalysts.

samples	T_{50} (°C)	T_{90} (°C)	T_{100} (°C)	R_s ($\mu\text{mol}/\text{min}\cdot\text{m}^2$)	E_a (kJ/mol)
LCO	271	283	297	1.31×10^{-3}	118.1
LCO-1.5 F	239	251	261	1.54×10^{-3}	96.1
LCO-2 F	226	238	245	4.92×10^{-3}	72.6
LCO-2.5 F	235	246	253	2.53×10^{-3}	90.2

Table 1. The R_s values of the F substituted LCO catalysts are significantly larger than that of pure LCO in toluene oxidation, attesting their improved intrinsic activity that is closely related to the mobility of surface O_{latt} species. In addition, the qualitative relationship between the T_{90} values and the $\text{Co}^{3+}/\text{Co}^{2+}$ ratio as well as the $\text{O}_{\text{latt}}/\text{O}_{\text{ads}}$ ratio of the as-prepared catalysts to visualize their correlation. As revealed in Fig. S6, a negative correlation between T_{90} values and the $\text{Co}^{3+}/\text{Co}^{2+}$ ratio as well as the $\text{O}_{\text{latt}}/\text{O}_{\text{ads}}$ ratio was found, illustrating that the catalytic activity of the as-prepared catalysts is closely related to the surface Co^{3+} species and the lattice oxygen.

Considering that catalytic stability is a vital indicator of catalyst for practical application. The long-term durability and cycling reusability of LCO-2 F were examined. As revealed in Fig. 4d, the toluene conversion at 240 °C is almost unaltered within 48 h on-stream, certifying its superb stability during the whole catalytic oxidation process. In addition, LCO-2 F also displays excellent cycling reusability, as substantiated by the similar light-off curves of toluene upon ten consecutive runs (Fig. 4e). As shown in Fig. S7, the used catalyst presents nearly identical states to the fresh one regard to the binding energy of Co and O elements, and relative amount of $\text{Co}^{3+}/\text{Co}^{2+}$ as well as $\text{O}_{\text{latt}}/\text{O}_{\text{ads}}$ (Table S2). Additionally, the used catalyst also reveals nearly uniform crystal structure compared with the fresh one (Fig. S8). Above results demonstrate that the surface of catalyst post-reaction remains well-retained. In view of widely presence of water vapor in the practical exhaust condition, the water-resistance of LCO-2 F was also investigated. As presented in Fig. 4f, introduction of 10 vol% H_2O into the feed gas generates a tiny suppression for the toluene conversion of LCO-2 F with a decrease by ca. 1% at 240 °C, as well the toluene conversion can be quickly restored to its original level when 10 vol% H_2O is turned off. Meanwhile, the water-resistance of LCO was also investigated as a comparison and shown in Fig. S9. when 10 vol% H_2O is injected into the feed gas, a more obvious inhibition with a decline by ca. 3% for the toluene conversion of LCO can be observed, illustrating its inferior water-resistance compared with that of LCO-2 F. This result may be due to two reasons. On the one hand,

LCO-2 F has more hydrophobic surface evidenced by its larger contact angle than that of LCO (Fig. S10). On the other hand, LCO-2 F reveals a stronger adsorption capacity towards the toluene molecules as a result of its more negative adsorption energy (Fig. 6d), which contributes to the competitive adsorption of toluene molecules against the H₂O molecules at the humid atmosphere. Furthermore, the light-off curve for LCO-2 F exhibits merely a slight degeneration in the presence of 10 vol% H₂O (Fig. S11). In brief, LCO-2 F possesses superb capacity for long-term operation and water-resistance that are requisite for the real application.

3.4. O_{latt} activity and toluene adsorption performance

In consideration of preceding deduction that the activation of surface O_{latt} could heighten the toluene oxidation. Consequently, the mobility of surface O_{latt} were emphatically investigated. H₂-TPR tests were first performed to inspect the reducibility of as-synthesized LCO catalysts and examine the utilizability of the surface O_{latt} . The profiles of H₂-TPR were presented in Fig. 5a. For pristine LCO, two reduction peaks emerge at approximately 420 °C and 650 °C, indicating the reduction of Co^{3+} to Co^{2+} and Co^{2+} to Co^0 [41], respectively. Following F incorporation, the peak for the reduction of Co^{3+} splits into two peaks. The former shifts to the lower temperature region that attributes to the better reducibility of Co^{3+} located at defect around [15], which may result from more formation of bulk oxygen vacancies and the weakened Co–O bond strength after F introduction. The latter should be ascribed to the reduction of remaining Co^{3+} . A lower reduction temperature reflects the stronger reducibility. Therefore, the reducibility of as-prepared catalysts consecutively raises in the sequence of LCO < LCO-1.5 F < LCO-2.5 F < LCO-2 F, which exhibits a positive correlation with their catalytic activity for toluene oxidation. Moreover, the H₂ consumptions of the catalysts below 500 °C were listed in Table S3. LCO-2 F reveals more H₂ consumptions followed by LCO-2.5 F, LCO-1.5 F and LCO, which is in

well accord with the content of surface Co^{3+} species, further evidencing the increased distribution of Co^{3+} species on the surface upon F incorporation.

O₂-TPD experiments were conducted to further discern the mobility of O_{latt} . As shown in Fig. 5b, the O₂-TPD profiles can be divided into three regions, corresponding to the physically and chemically O_{ads} (100–300 °C), surface O_{latt} (300–500 °C), and bulk O_{latt} (exceed 500 °C), respectively [42]. Notably, the desorption regarding surface O_{latt} over F substituted LCO moves to a lower temperature compared to LCO, and LCO-2 F reveals a minimum temperature centered at 393 °C among those catalysts, testifying that the surface O_{latt} over LCO-2 F is more active. Moreover, LCO-2 F also gives a better mobility involving the bulk O_{latt} , attributable to its more bulk oxygen vacancies, which avails to speedily replenish the exhausted surface O_{latt} and thus improving the catalytic oxidation cycle. The quantified amount of desorbed oxygen species is listed in Table S3. Besides the lower desorption temperature, the desorption amount of surface O_{latt} also increases with the F substitution, which is in agreement with the XPS result. Among them, LCO-2 F also presents a greater desorption amount than other catalysts. These results concurrently confirm that F incorporation enables the ample and active surface O_{latt} species over LCO-2 F to directly participate in toluene oxidation, and consequently rendering its more excellent catalytic activity.

It was usually accepted that the toluene is initially adsorbed on the catalyst surface followed by reacting with the surface O_{latt} in the toluene oxidation process. Accordingly, toluene-TPD with the absence of gaseous oxygen was performed to expressly determinate the toluene adsorption capacity and the activity of surface O_{latt} . Fig. 5c displays the desorption behavior of toluene in LCO and LCO-2 F as a function of temperature. The desorption behaviors at around 160 °C are attributed to the weakly adsorbed toluene. Obviously, the desorption peak for LCO-2 F appears at higher temperature of 165 °C as compared with the bare

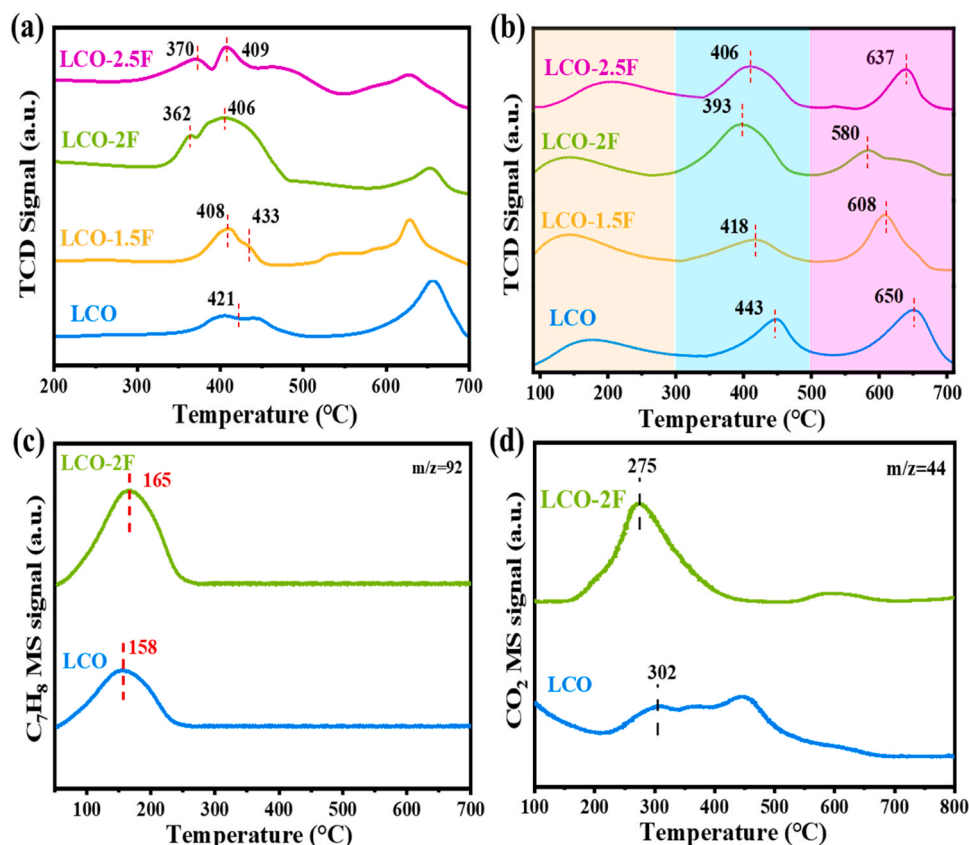


Fig. 5. (a) H₂-TPR profiles and (b) O₂-TPD profiles of the catalysts, (c) C₇H₈ MS signals and (d) CO₂ MS signals of LCO and LCO-2 F based on C₇H₈-TPD.

LCO that at 158 °C, illustrating that the LCO-2 F has a stronger interaction with toluene. Moreover, Fig. 5d presents the formation behaviors of CO₂ that are ascribed to the reaction of strong adsorbed toluene with the surface O_{latt} [43,44]. It is apparent that the CO₂ formation emerges at a lower temperature of 275 °C in LCO-2 F compared to the 302 °C in LCO, clarifying that the former reveals more easily generation of CO₂ resulted from the deep oxidation of toluene. Furthermore, the normalized quantities of the toluene desorption and CO₂ formation were presented in Fig. S12. Evidently, the LCO-2 F also exhibits larger amount of toluene desorption and CO₂ formation compared to that of pristine LCO, suggesting that LCO-2 F possesses a higher toluene adsorption capacity and more reactive surface O_{latt} to take part in the complete oxidation of toluene. It can thus be concluded that the highly distributive surface Co³⁺ species and weakened Co-O bond strength over LCO-2 F following F substitution significantly promote the toluene adsorption and the excitation of surface O_{latt}, which synergistically boost the catalytic performance of LCO-2 F.

3.5. DFT calculations

The electronic structures of LCO models before and after F substitution were further investigated to inspect the effect of F substitution on Co-O hybridization in LCO. The projected density of states (PDOS) on O 2p and Co 3d states of LCO model and F substituted LCO model were present in Fig. S13. The resonance peaks between O 2p and Co 3d at around -5.7, -3.2, -2.5, and -0.9 eV alleviate following F substitution, indicating a weaker Co-O hybridization that results in the reduced bonding interaction between O and Co atoms. This leads to a more facile liberation of the O_{latt} on the F substituted LCO surface, further attested by the lower formation energy of oxygen vacancy (E_{VO}). As shown in Fig. 6a and b, the E_{VO} of the F substituted LCO is recorded to be 0.13 eV, which is much lower than that of the bare LCO of 0.91 eV. In the meantime, the lengths of Co-O bond in LCO before and after F substitution were also obtained (Fig. S14). Unsurprisingly, the Co-O bond in F substituted LCO (1.98 Å) is longer than that of the bare LCO (1.96 Å). The aforementioned results suggest that the lattice oxygen can be effectively activated over the F substituted LCO. Moreover, the adsorption energies of toluene were predicted to verify the adsorptive performance of LCO and F substituted LCO for toluene molecule. As depicted in Fig. 6c and d, the adsorption energy of toluene (E_{ads-C₇H₈}) over LCO and F substituted LCO are -0.14 and -0.43 eV, respectively. The more negative adsorption energy means the stronger interaction between the

catalyst surface and the adsorbed molecule [45]. Besides, the charge density difference analysis was conducted on LCO and F substituted LCO with the adsorption of toluene. As displayed in Fig. 7, the yellow and green areas represent charge accumulation and charge depletion, respectively. More explicitly, the areas marked in the red dotted box reveal the electron transfer between toluene and the LCO surface (Fig. 7c and d). Obviously, the charge density difference analysis manifests that toluene molecule is more prone to give electron to the Co site on the LCO surface. More importantly, roughly 0.35 electrons transfer from the adsorbed toluene molecule to the F substituted LCO surface, which is higher than that of bare LCO (0.31 e) (Fig. 6d), suggesting the stronger interaction between toluene molecule and F substituted LCO [46,47]. This can be attributed to more electron-deficient Co³⁺ species distributed on LCO surface following the F incorporation that promote the charge transfer from toluene molecule to the catalyst surface. As a consequence, incorporation of F into LCO can incontestably enhance its adsorption and activation ability towards the toluene molecule. Overall, the computational results well conform to the experimental results.

3.6. Reaction mechanism for toluene oxidation

To further understand the reaction mechanism for toluene oxidation concerning the surface O_{latt}, in situ DRIFTS technique was employed to discern the key intermediate species during the adsorption and oxidation process of toluene over LCO and LCO-2 F. As presented in Fig. 8, the bands locate at around 3081, 3039, 2885, and 2936 cm⁻¹ can be ascribed to the phenylic C-H stretching vibration of the aromatic ring in toluene [48,49]. The band at around 2360 cm⁻¹ can be attributed to CO₂ [50]. The several feeble bands at 1944, 1865, and 1798 cm⁻¹ represent the characteristic bands of maleic anhydride [51]. The bands at around 1606 and 1457 cm⁻¹ belong to the C=O vibration peak subordinate to benzaldehyde and the vibration of the skeleton C-C bond derived from the benzene ring of benzaldehyde [52], respectively. The bands at around 1498 and 1390 cm⁻¹ can be designated as the anti-symmetric C-O stretching vibration and symmetric C-O stretching vibration of benzoate [53,54], respectively. In addition, a weak band at 1032 and 1077 cm⁻¹ corresponds to the benzyl alcohol [54].

Fig. 8a and b exhibited the time-resolved in situ DRIFTS spectra of LCO and LCO-2 F for toluene adsorption at 260 °C under oxygen-deficient conditions, respectively. The identically intermediate species can be observed over LCO and LCO-2 F, suggesting their consistent reaction pathway. Even so, the accumulation of intermediate species is of

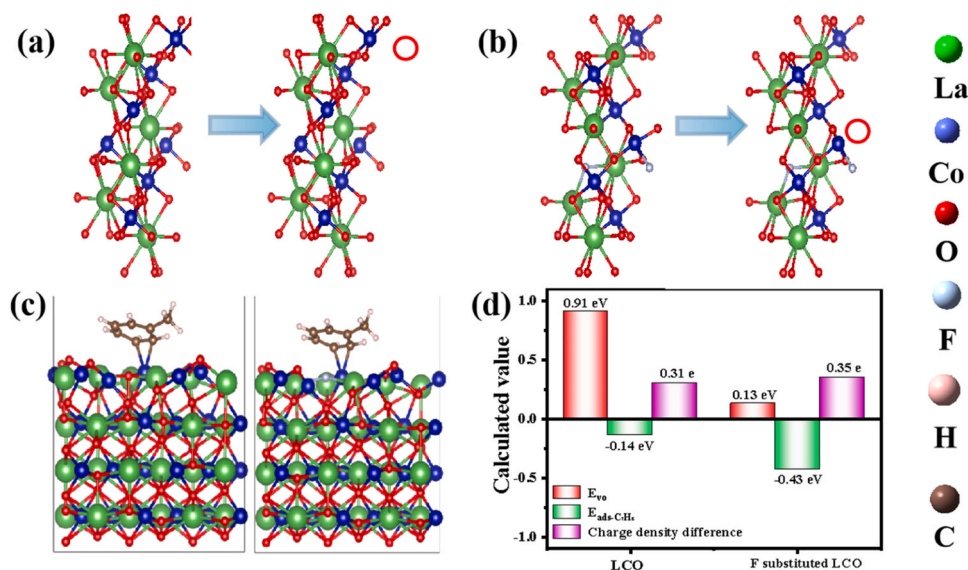


Fig. 6. (a) Oxygen vacancies formation energy of LCO and (b) F substituted LCO, (c) Toluene adsorption energy of LCO and F substituted LCO, and (d) Calculated result histogram of LCO and F substituted LCO.

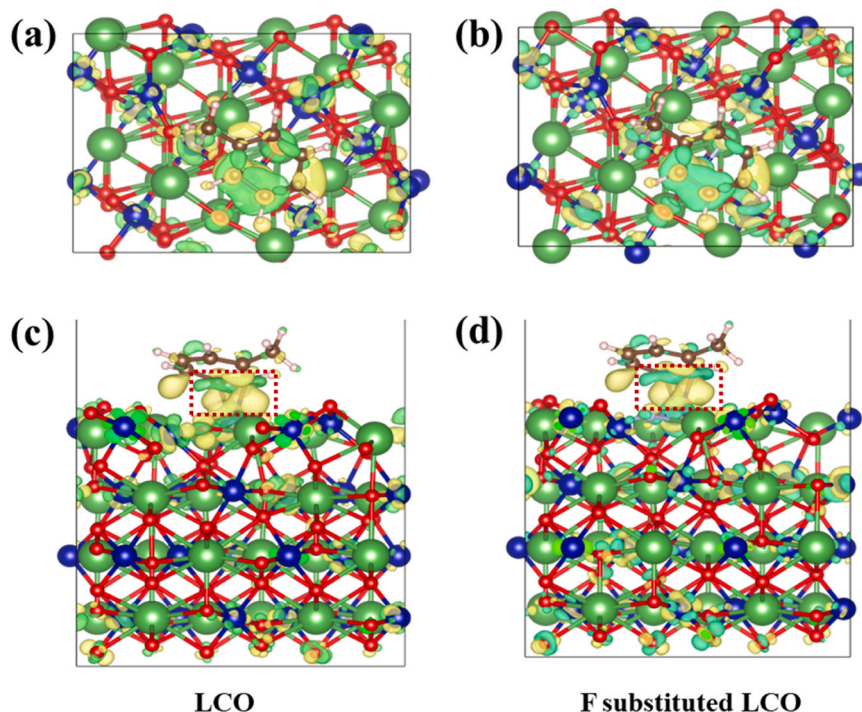


Fig. 7. Charge density difference ($\delta\rho = \rho_{A+B} - \rho_A - \rho_B$) of adsorbed toluene at Co site. View from (a, b) above and (c, d) side (Color scheme: La = green, F = grey, Co = blue, O = red).

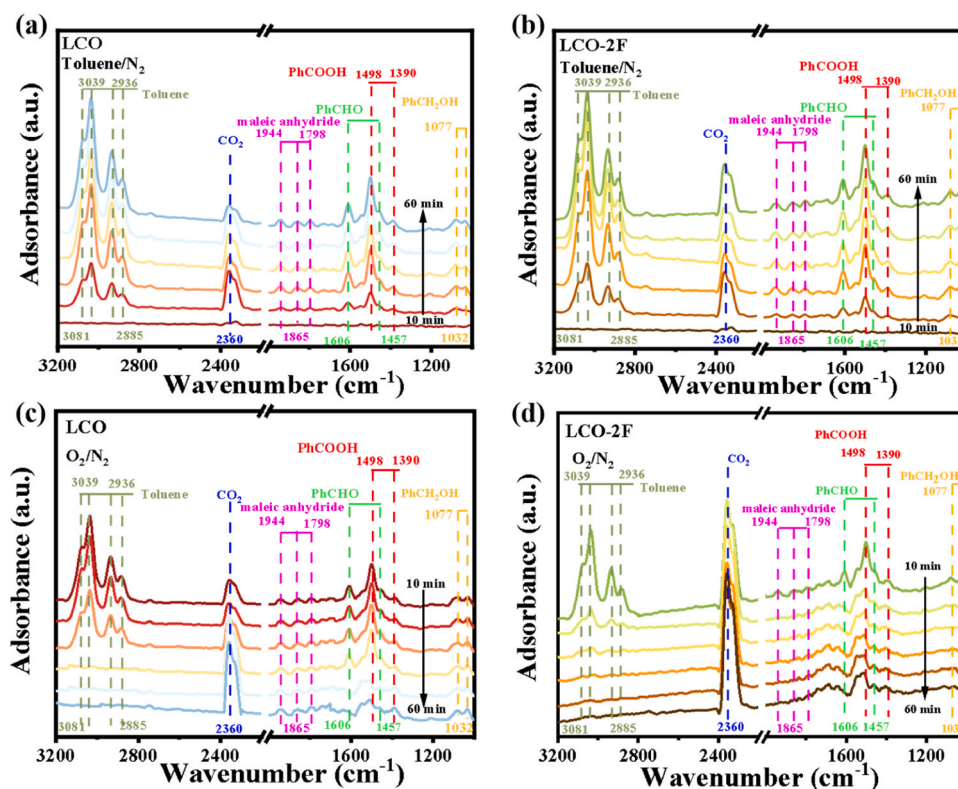


Fig. 8. In situ DRIFTS spectra of toluene adsorption as a function of time at 260 °C over (a) LCO and (b) LCO-2 F. In situ DRIFTS spectra of toluene oxidation as a function of time at 260 °C over (c) LCO and (d) LCO-2 F.

significant difference. The peak intensities of toluene present a much obviously increase in LCO-2 F compared to that in LCO, demonstrating its stronger adsorption ability for toluene. Additional, for LCO-2 F, the mineralization product of CO₂ is almost invariable within 60 min while

the amount of CO₂ gradually decreases for LCO with adsorption time, illustrating that LCO-2 F has more abundant and active surface O_{latt} to participate in the deep oxidation of toluene. Besides, the peak intensities of benzoate are stronger in LCO-2 F than that in LCO, suggesting its more

surface O_{latt} as well. Notably, more abundance of benzoate accumulation is observed than other intermediate species, such as benzyl alcohol, benzaldehyde, and maleic anhydride, declaring that the ring-opening, namely, further oxidation of benzoic acid is the formidable step existed usually in the toluene oxidation process [28,52]. For the oxidation process under oxygen-rich conditions (Fig. 8c and d), the adsorbed toluene over LCO-2 F quickly depletes within 20 min, whereas, it requires exceed 30 min for LCO. Likewise, benzoate in LCO-2 F is also more quickly consumed by reactive oxygen species stemmed from gaseous oxygen activation. Besides that, a larger CO_2 yield in LCO-2 F is given relative to that in LCO as well. These results prove that LCO-2 F reveals a more ready replenishing for the consumed lattice oxygen by activating the gaseous oxygen.

Furthermore, the peak areas of benzoate were normalized to vividly disclose the effect of the surface O_{latt} and the replenishing of gaseous oxygen on the toluene degradation. As shown in Fig. 9a, during the adsorption process, the accumulation of benzoate in LCO persistently increases while the accumulation of benzoate in LCO-2 F first rises and then fleetly tends to be saturated, implying the higher activity of surface O_{latt} in LCO-2 F. Moreover, in the oxidation process (Fig. 9b), the accumulation of benzoate in LCO remains stable at the initial 30 min and then decreases, whereas, the benzoate in LCO-2 F is rapidly removed once the gaseous oxygen introduction. This suggests that LCO-2 F possesses more excellent activation capacity towards gaseous oxygen so as to promote the total oxidation of toluene.

Based on the results of in situ DRIFTS, the reaction mechanism for toluene oxidation is proposed in Fig. 10. Specifically, toluene was first adsorbed in the highly distributed Co^{3+} sites of LCO-2 F and then reacted with the activated surface O_{latt} to generate a series of intermediate species containing benzyl alcohol, benzaldehyde, benzoate, and maleic anhydride, which accords with the MvK mechanism. Therein, the ring-opening of benzoate is regarded as the sluggish step, due to its more accumulation on the catalyst surface. Benefiting from the excellent replenishing of gaseous oxygen in LCO-2 F, the accumulated benzoate

can be fast mineralized to CO_2 and H_2O , and thus leading to an accelerated redox cycle.

4. Conclusion

In summary, a strategy of F substitution is proposed to greatly boost the catalytic performance of LCO perovskite oxide. In this work, the F ions can be inserted into the crystal lattice of LCO to substitute the O ions, which generates the significant variation in the geometrical and electronic structure of Co–O bond. Specifically, the elongated Co–O bond length and lower electron concentration surrounding the O_{latt} and Co sites can be obtained following the proper amount of F incorporation due to its highly electrophilic ability. These synergistically enables the weakening of Co–O bond strength, and thus the greatly improved reactivity of surface O_{latt} . Besides, the introduction of F induces more Co^{3+} species exposed on the catalyst surface as well, which enables the enhanced adsorption and activation towards toluene molecule. By virtue of the above merits, LCO-2 F reveals a maximum catalytic activity and excellent catalytic stability as well as water-resistance. This scheme can also be generalized to fabricate other perovskite oxides for VOCs combustion.

CRediT authorship contribution statement

Luo Xubiao: Writing – review & editing. **Wu Keshi:** Conceptualization, Writing – review & editing. **Zou Jianping:** Visualization, Writing – review & editing. **Zhang Jie:** Validation. **Zhou Lei:** Visualization. **Huang Zhilong:** Validation, Visualization. **Zhong Xiaolian:** Validation, Visualization. **Xiong Hao:** Investigation, Methodology, Validation, Visualization. **Dai Weili:** Funding acquisition, Supervision, Writing – review & editing. **Li Bing:** Conceptualization, Funding acquisition, Investigation, Methodology, Writing – original draft.

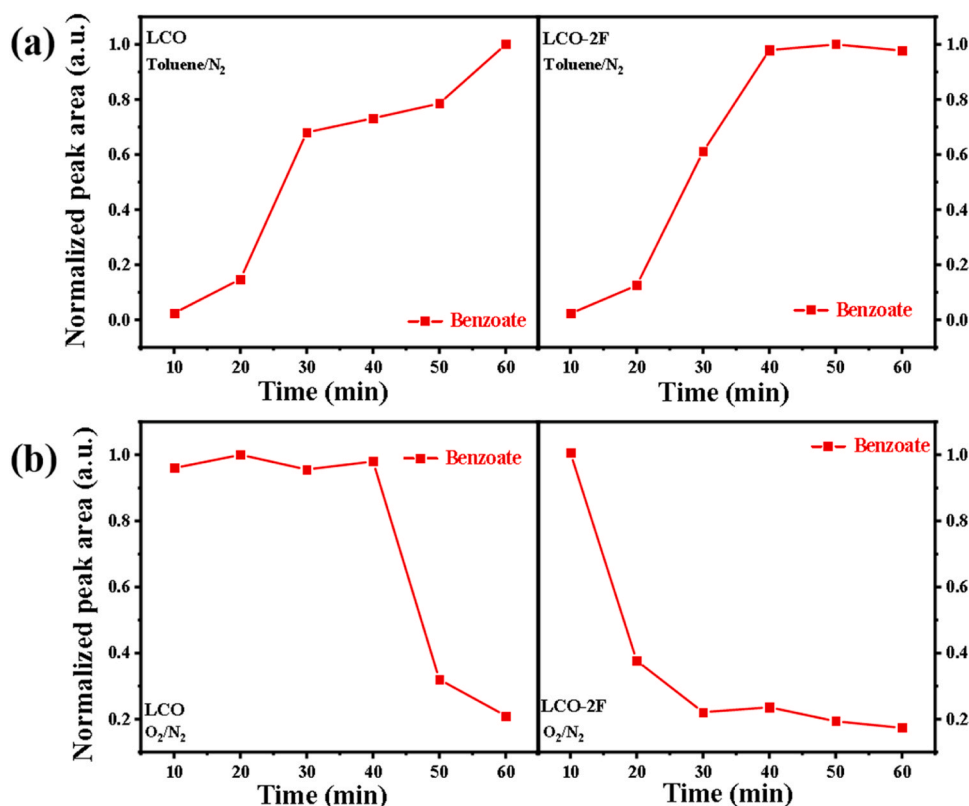


Fig. 9. (a) Plots of accumulation of the benzoate for the toluene adsorption and (b) Plots of consumption of the benzoate for the toluene.

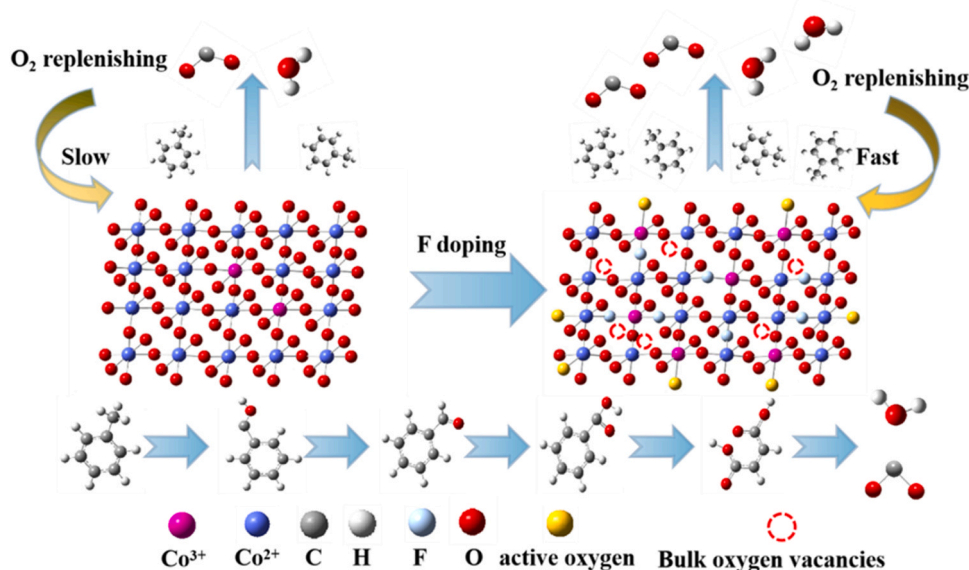


Fig. 10. The proposed toluene degradation mechanism over LCO and LCO-2 F.

Declaration of Competing Interest

The authors declare that they have no known competing financial interests or personal relationships that could have appeared to influence the work reported in this paper.

Data Availability

Data will be made available on request.

Acknowledgements

This work was supported by the National Natural Science Foundation of China (Grant Nos. 52360015), and Key Research and Development Program of Jiangxi Province (Grant Nos. 20192ACB70009).

Appendix A. Supporting information

Supplementary data associated with this article can be found in the online version at [doi:10.1016/j.apcatb.2024.123828](https://doi.org/10.1016/j.apcatb.2024.123828).

References

- [1] H. Wang, Q. Wang, Y. Gao, M. Zhou, S. Jing, L. Qiao, B. Yuan, D. Huang, C. Huang, S. Lou, R. Yan, J.A. Gouw, X. Zhang, J. Chen, C. Chen, S. Tao, J. An, Y. Li, Estimation of secondary organic aerosol formation during a photochemical smog episode in Shanghai, China, *e2019JD032033*, *J. Geophys. Res.-Atmos.* 125 (2020), <https://doi.org/10.1029/2019jd032033>.
- [2] Q. Sha, M. Zhu, H. Huang, Y. Wang, Z. Huang, X. Zhang, M. Tang, M. Lu, C. Chen, B. Shi, Z. Chen, L. Wu, Z. Zhong, C. Li, Y. Xu, F. Yu, G. Jia, S. Liao, X. Cui, J. Liu, J. Zheng, A newly integrated dataset of volatile organic compounds (VOCs) source profiles and implications for the future development of VOCs profiles in China, *Sci. Total Environ.* 793 (2021) 148348, <https://doi.org/10.1016/j.scitotenv.2021.148348>.
- [3] N. Afshar-Mohajer, M.A. Fox, K. Koehler, The human health risk estimation of inhaled oil spill emissions with and without adding dispersant, *Sci. Total Environ.* 654 (2019) 924, <https://doi.org/10.1016/j.scitotenv.2018.11.110>.
- [4] Y. Zheng, Y. Su, C. Pang, L. Yang, C. Song, N. Ji, D. Ma, X. Lu, R. Han, Q. Liu, Interface-enhanced oxygen vacancies of CoCuO_x catalysts in situ grown on monolithic Cu foam for VOC catalytic oxidation, *Environ. Sci. Technol.* 56 (2022) 1905–1916, <https://doi.org/10.1021/acs.est.1c05855>.
- [5] S. Royer, D. Duprez, F. Can, X. Courtois, C. Batiot-Dupeyrat, S. Laassiri, H. Alamdari, Perovskites as substitutes of noble metals for heterogeneous catalysis: dream or reality, *Chem. Rev.* 114 (2014) 10292–10368, <https://doi.org/10.1021/cr500032a>.
- [6] L. Zhang, Y.J. Liu, X. Fang, Y. Cheng, Regulating oxygen species for promoted deep oxidation of toluene: a comparative study of adsorbed oxygen and lattice oxygen, *Fuel* 321 (2022) 124116, <https://doi.org/10.2139/ssrn.3986912>.
- [7] Q. Chen, Z. Wang, X. Wang, J. Li, Y. Li, G. Zhang, A novel Cu_{1.5}Mn_{1.5}O₄ photothermal catalyst with boosted surface lattice oxygen activation for efficiently photothermal mineralization of toluene, *Nano Res.* 16 (2022) 2133–2141, <https://doi.org/10.2139/ssrn.4051632>.
- [8] H. Zhu, P. Zhang, S. Dai, Recent advances of lanthanum-based perovskite oxides for catalysis, *ACS Catal.* 5 (2015) 6370–6385, <https://doi.org/10.1021/acscatal.5b01667>.
- [9] G. Xiao, S. Xin, H. Wang, R. Zhang, Q. Wei, Y. Lin, Catalytic oxidation of styrene over Ce-substituted La_{1-x}Ce_xMnO₃ catalysts, *Ind. Eng. Chem. Res.* 58 (2019) 5388–5396, <https://doi.org/10.1021/acs.iecr.8b05674>.
- [10] B. Heidinger, S. Royer, J. Giraudon, O. Gardoll, H. Alamdari, J. Lamonier, Reactive grinding synthesis of La(Sr,Ce)CoO₃ and their properties in toluene catalytic total oxidation, *ChemCatChem* 12 (2020) 2271–2282, <https://doi.org/10.1002/cctc.201902112>.
- [11] K. Hashimoto, R. Otomo, Y. Kamiya, SrFe_{1-x}Sn_xO_{3-δ} nanoparticles with enhanced redox properties for catalytic combustion of benzene, *Catal. Sci. Technol.* (18) (2020) 6342–6349, <https://doi.org/10.1039/d0cy01154a>.
- [12] Y. Xu, J. Dhainaut, J.P. Dacquin, A.S. Mamede, M. Marinova, J.F. Lamonier, H. Vezin, H. Zhang, S. Royer, La_{1-x}(Sr, Na, K)_xMnO₃ perovskites for HCHO oxidation: the role of oxygen species on the catalytic mechanism, *Appl. Catal. B Environ.* 287 (2021) 119955, <https://doi.org/10.1016/j.apcatb.2021.119955>.
- [13] Y. Luo, Y. Zheng, X. Feng, D. Lin, Q. Qian, X. Wang, Y. Zhang, Q. Chen, X. Zhang, Controllable P doping of the LaCoO₃ catalyst for efficient propane oxidation: optimized surface Co distribution and enhanced oxygen vacancies, *ACS Appl. Mater. Interfaces* (21) (2020) 23789–23799, <https://doi.org/10.1021/acsaami.0c01599>.
- [14] M. Wu, S. Chen, W. Xiang, Oxygen vacancy induced performance enhancement of toluene catalytic oxidation using LaFeO₃ perovskite oxides, *Chem. Eng. J.* 387 (2020) 124101, <https://doi.org/10.1016/j.cej.2020.124101>.
- [15] C. Feng, Q. Gao, G. Xiong, Y. Chen, Y. Pan, Z. Fei, Y. Li, Y. Lu, C. Liu, Y. Liu, Defect engineering technique for the fabrication of LaCoO₃ perovskite catalyst via urea treatment for total oxidation of propane, *Appl. Catal. B Environ.* 304 (2022) 121005, <https://doi.org/10.1016/j.apcatb.2021.121005>.
- [16] M. Wu, S. Ma, S. Chen, W. Xiang, Fe–O terminated LaFeO₃ perovskite oxide surface for low temperature toluene oxidation, *J. Clean. Prod.* 277 (2020) 123224, <https://doi.org/10.1016/j.jclepro.2020.123224>.
- [17] Y. Liu, H. Hu, F. Xie, H. Gu, S. Rostamnia, F. Pan, X. Liu, L. Zhang, Interfacial engineering enables surface lattice oxygen activation of SmMn₂O₅ for catalytic propane combustion, *Appl. Catal. B Environ.* 330 (2023) 122649, <https://doi.org/10.1016/j.apcatb.2023.122649>.
- [18] X. Wang, Z. Pan, X. Chu, K. Huang, Y. Cong, R. Cao, R. Sarangi, L. Li, G. Li, S. Feng, Atomic-scale insights into surface lattice oxygen activation at the spinel/perovskite interface of Co₃O₄/La_{0.3}Sr_{0.7}CoO₃, *Angew. Chem. Int. Ed.* 58 (2019) 11720–11725, <https://doi.org/10.1002/anie.201905543>.
- [19] B. Yang, M. Zhang, Y. Zeng, F. Meng, J. Ma, S. Zhang, Q. Zhong, Promotional effect of surface fluorine species on CeO₂ catalyst for toluene oxidation, *Mol. Catal.* 512 (2021) 111771, <https://doi.org/10.1016/j.mcat.2021.111771>.
- [20] X. Yu, M. Shi, Y. Fan, L. Yang, J. Zhang, W. Liu, W. Dai, S. Zhang, L. Zhou, X. Luo, S. Luo, Activation or passivation: Influence of halogen dopant (F, Cl, Br) on photothermal activity of Mn₂O₃ in degrading toluene, *Appl. Catal. B Environ.* 309 (2022) 121236, <https://doi.org/10.1016/j.apcatb.2022.121236>.
- [21] Q. Yang, D. Wang, C. Wang, X. Li, K. Li, Y. Peng, J. Li, Facile surface improvement method for LaCoO₃ for toluene oxidation, *Catal. Sci. Technol.* (12) (2018) 3166–3173, <https://doi.org/10.1039/c8cy00765a>.

- [22] C. Yang, Y. Tian, J. Pu, B. Chi, Anion fluorine-doped $\text{La}_{0.6}\text{Sr}_{0.4}\text{Fe}_{0.8}\text{Ni}_{0.2}\text{O}_{3-\delta}$ perovskite cathodes with enhanced electrocatalytic activity for solid oxide electrolysis cell direct CO_2 electrolysis, *ACS Sustain. Chem. Eng.* 10 (2022) 1047–1058, <https://doi.org/10.1021/acsschemeng.1c07576>.
- [23] Z. Li, W. Niu, Z. Yang, N. Zaman, W. Samarakoon, M. Wang, A. Kara, M. Lucero, M. V. Vyas, H. Cao, H. Zhou, G.E. Sterbinsky, Z. Feng, Y. Du, Y. Yang, Stabilizing atomic Pt with trapped interstitial F in alloyed PtCo nanosheets for high-performance zinc-air batteries, *Energy Environ. Sci.* 13 (2020) 884–895, <https://doi.org/10.1039/C9EE02657F>.
- [24] Y. Zhang, Q. Li, Y. Long, J. Cao, Z. Song, C. Liu, L. Liu, F. Qi, B. Xu, Z. Chen, Catalytic ozonation benefit from the enhancement of electron transfer by the coupling of $\text{g-C}_3\text{N}_4$ and LaCoO_3 : discussion on catalyst fabrication and electron transfer pathway, *Appl. Catal. B Environ.* 254 (2019) 569–579, <https://doi.org/10.1016/j.apcatb.2019.05.019>.
- [25] J. Xiong, H. Zhong, J. Li, X. Zhang, J. Shi, W. Cai, K. Qu, C. Zhu, Z. Yang, S. P. Beckman, H. Cheng, Engineering highly active oxygen sites in perovskite oxides for stable and efficient oxygen evolution, *Appl. Catal. B Environ.* 256 (2019) 117817, <https://doi.org/10.1016/j.apcatb.2019.117817>.
- [26] X. Zhang, B. Li, L. Shen, Y. Cao, Y. Zhan, S. Zheng, S. Wang, L. Jiang, Oxygen vacancies engineering of Fe doped LaCoO_3 perovskite catalysts for efficient H_2S selective oxidation, *Appl. Catal. B Environ.* 329 (2023) 122526, <https://doi.org/10.1016/j.apcatb.2023.122526>.
- [27] Y. Zhang, H. Liu, H. Hu, R. Xie, G. Ma, J. Huo, H. Wang, Orientation-dependent structural and photocatalytic properties of LaCoO_3 epitaxial nano-thin films, *Roy. Soc. Open Sci.* 5 (2018) 171376, <https://doi.org/10.1098/rsos.171376>.
- [28] Y. Shen, J. Deng, S. Impeng, S. Li, T. Yan, J. Zhang, L. Shi, D. Zhang, Boosting toluene combustion by engineering Co-O strength in cobalt oxide catalysts, *Environ. Sci. Technol.* 54 (2020) 10342–10350, <https://doi.org/10.1021/acs.est.0c02680>.
- [29] W. Xie, G. Xu, Y. Zhang, Y. Yu, H. He, Mesoporous LaCoO_3 perovskite oxide with high catalytic performance for NO storage and reduction, *J. Hazard. Mater.* 431 (2022) 128528, <https://doi.org/10.1016/j.jhazmat.2022.128528>.
- [30] Z. Gao, J. Zhang, S. Zhang, J. Wang, Y. Song, Cationic etching of ZIF-67 derived $\text{LaCoO}_3/\text{Co}_3\text{O}_4$ as high-efficiency electromagnetic absorbers, *Chem. Eng. J.* 421 (2021) 127829, <https://doi.org/10.1016/j.cej.2020.127829>.
- [31] J. Huang, K. Wang, X. Huang, J. Huang, Deep oxidation of benzene over LaCoO_3 catalysts synthesized via a salt-assisted sol-gel process, *Mol. Catal.* 493 (2020) 111073, <https://doi.org/10.1016/j.mcat.2020.111073>.
- [32] J. Zhong, Y. Zeng, D. Chen, S. Mo, M. Zhang, M. Fu, J. Wu, Z. Su, P. Chen, D. Ye, Toluene oxidation over Co^{3+} -rich spinel Co_3O_4 : evaluation of chemical and by-product species identified by in situ DRIFTS combined with PTR-TOF-MS, *J. Hazard. Mater.* 386 (2020) 121957, <https://doi.org/10.1016/j.jhazmat.2019.121957>.
- [33] M. Klaus, K. Kasper, The chemical bond between transition metals and oxygen: electronegativity, d-orbital effects, and oxophilicity as descriptors of metal–oxygen interactions, *J. Phys. Chem. C* 123 (2019) 18432–18444, <https://doi.org/10.1021/acs.jpcc.9b04317>.
- [34] D. Bergmann, H. Juerge, Electronegativity and molecular properties, *Angew. Chem. Int. Ed. Engl.* 35 (1996) 150–163, <https://doi.org/10.1002/anie.199601501>.
- [35] P. Li, Y. Lin, S. Zhao, Y. Fu, W. Li, R. Chen, S. Tian, Defect-engineered Co_3O_4 with porous multishelled hollow architecture enables boosted advanced oxidation processes, *Appl. Catal. B Environ.* 298 (2021) 120596, <https://doi.org/10.1016/j.apcatb.2021.120596>.
- [36] L. Liu, J. Li, H. Zhang, L. Li, P. Zhou, X. Meng, M. Guo, J. Jia, T. Sun, In situ fabrication of highly active $\gamma\text{-MnO}_2/\text{SmMnO}_3$ catalyst for deep catalytic oxidation of gaseous benzene, ethylbenzene, toluene, and o-xylene, *J. Hazard. Mater.* 362 (2019) 178–186, <https://doi.org/10.1016/j.jhazmat.2018.09.012>.
- [37] B. Li, F. Deng, Z. Li, H. Xiong, S. Zhang, W. Dai, J. Zhang, L. Yang, J. Zou, X. Luo, Engineering Ag–O–Mn bridges with enhanced oxygen mobility over Ag substituted LaMnO_3 perovskite catalyst for robustly boosting toluene combustion, *Sep. Purif. Technol.* 320 (2023) 124240, <https://doi.org/10.1016/j.seppur.2023.124240>.
- [38] Y. Wang, J. Cai, M. Wu, J. Chen, W. Zhao, Y. Tian, T. Ding, J. Zhang, Z. Jiang, X. Li, Rational construction of oxygen vacancies onto tungsten trioxide to improve visible light photocatalytic water oxidation reaction, *Appl. Catal. B Environ.* 239 (2018) 398–407, <https://doi.org/10.1016/j.apcatb.2018.08.029>.
- [39] Z. Su, W. Yang, C. Wang, S. Xiong, X. Cao, Y. Peng, W. Si, Y. Weng, M. Xue, J. Li, Roles of oxygen vacancies in the bulk and surface of CeO_2 for toluene catalytic combustion, *Environ. Sci. Technol.* 54 (2020) 12684–12692, <https://doi.org/10.1021/acs.est.0c03981>.
- [40] M. Li, C. Zhang, L. Fan, Y. Lian, X. Niu, Y. Zhu, Enhanced catalytic oxidation of toluene over manganese oxide modified by lanthanum with a coral-like hierarchical structure nanosphere, *ACS Appl. Mater. Interfaces* 13 (2021) 10089–10100, <https://doi.org/10.1021/acsami.0c22297>.
- [41] R. Ao, L. Ma, Z. Guo, H. Liu, J. Yang, X. Yin, Q. Pan, Effects of the preparation method on the simultaneous catalytic oxidation performances of LaCoO_3 perovskites for NO and Hg^0 , *Fuel* 305 (2021) 121617, <https://doi.org/10.1016/j.fuel.2021.121617>.
- [42] M. Xiao, X. Yang, Y. Peng, Y. Guo, Y. Wei, M. Ge, X. Yu, Confining shell-sandwiched Ag clusters in $\text{MnO}_2\text{-CeO}_2$ hollow spheres to boost activity and stability of toluene combustion, *Nano Res.* 15 (2022) 7042–7051, <https://doi.org/10.1007/s12274-022-4360-0>.
- [43] Y. Zeng, K.G. Haw, Z. Wang, Y. Wang, S. Zhang, P. Hongmanorom, Q. Zhong, S. Kawi, Double redox process to synthesize CuO-CeO_2 catalysts with strong Cu–Ce interaction for efficient toluene oxidation, *J. Hazard. Mater.* 404 (2021) 124088, <https://doi.org/10.1016/j.jhazmat.2020.124088>.
- [44] W. Yang, Z. Su, Z. Xu, W. Yang, Y. Peng, J. Li, Comparative study of α -, β -, γ - and $\delta\text{-MnO}_2$ on toluene oxidation: Oxygen vacancies and reaction intermediates, *Appl. Catal. B Environ.* 260 (2020) 118150, <https://doi.org/10.1016/j.apcatb.2019.118150>.
- [45] X. Zhang, Y. Yang, Q. Zhu, M. Ma, Z. Jiang, X. Liao, C. He, Unraveling the effects of potassium incorporation routes and positions on toluene oxidation over $\alpha\text{-MnO}_2$ nanorods: Based on experimental and density functional theory (DFT) studies, *J. Colloid Interf. Sci.* 598 (2021) 324–338, <https://doi.org/10.1016/j.jcis.2021.04.053>.
- [46] J. Chen, S. Xiong, H. Liu, J. Shi, J. Mi, H. Liu, Z. Gong, L. Oliviero, F. Maugé, J. Li, Reverse oxygen spillover triggered by CO adsorption on Sn-doped Pt/ TiO_2 for low-temperature CO oxidation, *Nat. Commun.* 13 (2023) 3477, <https://doi.org/10.1038/s41467-023-39226-6>.
- [47] S. Zhao, Y. Wen, X. Liu, X. Pen, F. Lü, F. Gao, X. Xie, C. Du, H. Yi, D. Kang, X. Tang, Formation of active oxygen species on single-atom Pt catalyst and promoted catalytic oxidation of toluene, *Nano Res.* 13 (2020) 1544–1551, <https://doi.org/10.1007/s12274-020-2765-1>.
- [48] S. Zhao, K. Li, S. Jiang, J. Li, Pd–Co based spinel oxides derived from Pd nanoparticles immobilized on layered double hydroxides for toluene combustion, *Appl. Catal. B Environ.* 181 (2016) 236–248, <https://doi.org/10.1016/j.apcatb.2015.08.001>.
- [49] Q. Cheng, K. Kang, Y. Li, J. Wang, Z. Wang, D. Selishchev, X. Wang, G. Zhang, Achieving efficient toluene mineralization over ordered porous LaMnO_3 catalyst: the synergistic effect of high valence manganese and surface lattice oxygen, *Appl. Surf. Sci.* 615 (2023) 156248, <https://doi.org/10.1016/j.apsusc.2022.156248>.
- [50] S.I. Suárez-Vázquez, E.J. Moreno-Román, R. Zanella, A. Cruz-López, C. García-Gómez, A. Nieto-Márquez, S. Gil, Insight into the surface reaction mechanism of toluene oxidation over a composite $\text{CeO}_x/\text{La}_{1-x}\text{Ce}_x\text{MnO}_3$ catalyst using Drifts, *Chem. Eng. Sci.* 259 (2022) 117831, <https://doi.org/10.1016/j.ces.2022.117831>.
- [51] J. Zhong, Y. Zeng, M. Zhang, W. Feng, D. Xiao, J. Wu, P. Chen, M. Fu, D. Ye, Toluene oxidation process and proper mechanism over Co_3O_4 nanotubes: investigation through in-situ DRIFTS combined with PTR-TOF-MS and quasi in-situ XPS, *Chem. Eng. J.* 397 (2020) 125375, <https://doi.org/10.1016/j.cej.2020.125375>.
- [52] M. Xiao, X. Yu, Y. Guo, M. Ge, Boosting toluene combustion by tuning electronic metal–support interactions in situ grown Pt on Co_3O_4 catalysts, *Environ. Sci. Technol.* 56 (2022) 1376–1385, <https://doi.org/10.1021/acs.est.1c07016>.
- [53] L. Zhao, Z. Zhang, Y. Li, X. Leng, T. Zhang, F. Yuan, X. Niu, Y. Zhu, Synthesis of Ce_xMnO_x hollow microsphere with hierarchical structure and its excellent catalytic performance for toluene combustion, *Appl. Catal. B Environ.* 245 (2019) 502–512, <https://doi.org/10.1016/j.apcatb.2019.01.005>.
- [54] X. Yang, X. Yu, M. Jing, W. Song, J. Liu, M. Ge, Defective $\text{Mn}_x\text{Zr}_{1-x}\text{O}_2$ solid solution for the catalytic oxidation of toluene: insights into the oxygen vacancy contribution, *ACS Appl. Mater. Interfaces* 11 (2019) 730–739, <https://doi.org/10.1021/acsami.8b17062>.